Journal of Palaeogeography

ORIGINAL ARTICLE Open Access

Growth mechanisms and environmental implications of carbonate concretions from the ~ 1.4 Ga Xiamaling Formation, North China

An-Qi Liu[1,2], Dong-Jie Tang[1,2*], Xiao-Ying Shi[1,3], Li-Min Zhou[4], Xi-Qiang Zhou[5], Mo-Han Shang[3], Yang Li[3] and Hu-Yue Song[6]

Abstract

Carbonate concretions provide unique records of ancient biogeochemical processes in marine sediments, and have the potential to reflect seawater chemistry indirectly. In fine-siliciclastic settings, they preferentially form in organic-rich mudstones, owing to a significant fraction of the bicarbonate required for carbonate precipitation resulted from the decomposition of organic matter in sediments. In the Member IV of the Xiamaling Formation (*ca.* 1.40–1.35 Ga), North China, however, carbonate concretions occur in organic-poor green silty shales (avg. TOC = ~ 0.1 wt%). In order to elucidate the mechanism of the concretion formation and their environmental implications, a thorough study on the petrographic and geochemical compositions of the concretions and their host rocks was conducted. Macro- to microscopic fabrics, including deformed shale laminae surrounding the concretions, "cardhouse" structures of clay minerals and calcite geodes in the concretions, indicate that these concretions are of early diagenetic origin prior to the significant compaction of clay minerals. The carbon isotope compositions of the concretions (− 1.7‰ to + 1.5‰) are stable and close to or slightly lower than that of the contemporaneous seawater, indicating that the bicarbonates required for the concretion formation were mainly sourced from seawater by diffusion rather than produced by methanogenesis or anoxic oxidation of methane (AOM); the rare occurrence of authigenic pyrite grains in the concretions likely indicates that bacterial sulfate reduction (BSR) did not play a significant role in their formation either. Almost all the calcite in the concretions has low Mn–Fe in nuclei but high Mn–Fe in rims with average Mn/Fe ratio close to 3.3. The calcite shows positive Ce anomalies (avg. 1.43) and low Y/Ho ratios (avg. 31). This evidence suggests that Mn reduction is the dominant process responsible for the formation of calcite rims while nitrate reduction probably triggered the precipitation of calcite nuclei. Prominence of Mn reduction in the porewater likely indicates that there was sufficient oxygen to support active Mn-redox cycling in the overlying seawater.

Keywords: Mid-Proterozoic, Carbonate concretion, Early diagenesis, Manganese reduction, Bicarbonate

* Correspondence: dongjtang@126.com
[1]State Key Laboratory of Biogeology and Environmental Geology, China University of Geosciences (Beijing), Beijing 100083, China
[2]Institute of Earth Sciences, China University of Geosciences (Beijing), Beijing 100083, China
Full list of author information is available at the end of the article

1 Introduction

Early diagenetic carbonate concretions are authigenic mineral aggregates formed in sediments at the expense of microbial respiration of organic matter (e.g. Sellés-Martínez 1996; Raiswell and Fisher 2000; Gaines and Vorhies 2016). Various microbial processes in suboxic to anoxic zones of marine sediments have the ability to induce the formation of carbonate concretions by increasing the environmental alkalinity and *p*H (Curtis et al. 1986; Loyd et al. 2012). In different diagenetic zones, with the increase of burial depth, these processes may include nitrate reduction, manganese reduction, dissimilatory iron reduction (DIR), bacterial sulfate reduction (BSR), anoxic oxidation of methane (AOM), and methanogenesis. The locations of these processes and thicknesses of the resulting material depend largely on the availability of oxidants and organic matter (Roberts and Weaver 2005; Canfield and Thamdrup 2009; Loyd et al. 2012; Dong et al. 2013). However, among these processes, denitrification and Mn reduction processes have been commonly identified in marine sediments (Haley et al. 2004; Meyer et al. 2005) but rarely regarded as the dominant processes for the formation of carbonate concretions (e.g. Curtis et al. 1986; Canfield et al. 1993; Thamdrup and Canfield 1996; Raiswell and Fisher 2000; Loyd et al. 2012). Although reasons for this have not been fully addressed, low concentrations of nitrate, nitrite, and Mn-hydroxides in sediments of most environments were often quoted as the potential causes.

Early diagenetic carbonate concretions may record ancient biogeochemical processes and the porewater chemistry (e.g. Curtis et al. 1986; Raiswell and Fisher 2000; Hendry et al. 2006; Loyd et al. 2012). In recent years, multiple approaches have been used to decipher the potential of microbial processes for their formation, of which analysis of mineralogy, C–S isotopes and REE are principal aspects (e.g. Haley et al. 2004; Hendry et al. 2006; Loyd et al. 2012; Dong et al. 2013). Because different biochemical reactions dominate in different diagenetic zones, the ion concentrations, such as Mn^{2+}, Fe^{2+}, and HS^{-}, should be different (Canfield and Thamdrup 2009), and thus characteristic minerals could be formed in different diagenetic zones. For instance, calcite with high Mn/Fe ratio usually dominates in a Mn reduction zone (e.g. Curtis et al. 1986; Loyd et al. 2012), ankerite and siderite more often occur in an iron reduction and methanogenesis zone (e.g. Tang et al. 2018), while pyrite commonly concentrates in a sulfate reduction zone (e.g. Gaines and Vorhies 2016). Because the formation of carbonate concretion is commonly facilitated by partial incorporation of bicarbonate from the decomposition of organic matter, carbonate concretions preferentially occur in organic-rich mudstone settings and generally have their carbon isotope composition lower than that of contemporaneous seawaters. The extremely low carbon isotope composition of carbonate concretions (e.g. -110‰ to − 30‰; Whiticar 1999), has been recognized as the signature for AOM (e.g. Liang et al. 2016), while variable but commonly positive carbon isotope values (e.g. -30‰ to + 15‰) have been identified as the mark of methanogenesis (Raiswell and Fisher 2000). However, it is difficult to distinguish the other diagenetic processes solely based on carbon isotopes, since the values generated by them are often mutually overlapping. Fe–Mn-hydroxides are often regarded as one of the significant carriers of REE and commonly show high REE concentrations. Their reduction and dissolution would significantly influence the REE composition of pore fluids and could subsequently be recorded by the carbonate concretions formed in these zones (Haley et al. 2004). For example, a middle-REE (MREE) enriched pattern commonly occurs in a Fe-reduction zone (Haley et al. 2004), while positive Ce anomalies often exist in a Mn-reduction zone (Tostevin et al. 2016).

The availability of oxidants for biochemical reactions during early diagenesis is profoundly influenced by the overlying seawater chemistry. In turn, early diagenetic concretions may provide valuable insight into seawater chemistry. For example, in modern oceans the average sulfate concentration is as high as 28 mM (Lowenstein et al. 2001), therefore, during early diagenetic stage BSR is commonly the predominant process in sediments (e.g. Baumgartner et al. 2006). On the contrary, due to the overall low atmospheric oxygen level in mid-Proterozoic time (*ca.* 1.8–0.8 Ga) (< 0.1%–1% PAL, Lyons et al. 2014; Planavsky et al. 2014; Cole et al. 2016) the sulfate input from terrestrial weathering is presumed low, thus the sulfate concentration in the ocean was very low (< 1.8 mM; e.g. Kah et al. 2004; Luo et al. 2015). Under this circumstance, BSR process in marine sediments was not as prominent as that in modern oceans. If this is the case, most mid-Proterozoic carbonate concretions would record far less prominent BSR process with seldom authigenic pyrites. However, early diagenetic carbonates in ancient sediments have rarely been applied to reconstruct overlying seawater chemistry (Curtis et al. 1986; Raiswell and Fisher 2000; Hendry et al. 2006; Loyd et al. 2012; Dong et al. 2013).

In the middle part of the Member IV of the Xiamaling Formation (*ca.* 1.35–1.40 Ga) of North China Platform, abundant carbonate concretions occur in a ~ 6-m-thick interval of organic-poor green silty shale (Figs. 1 and 2). To reveal their growth mechanism and the potential environmental significance, the concretions have been thoroughly studied from petrography, mineralogy and geochemistry.

2 Geological setting

In this paper, we deal with carbonate concretions from the Member IV of the Xiamaling Formation in the North China Platform (Fig. 1). The Xiamaling Formation lies disconformably between the underlying Tieling Formation of

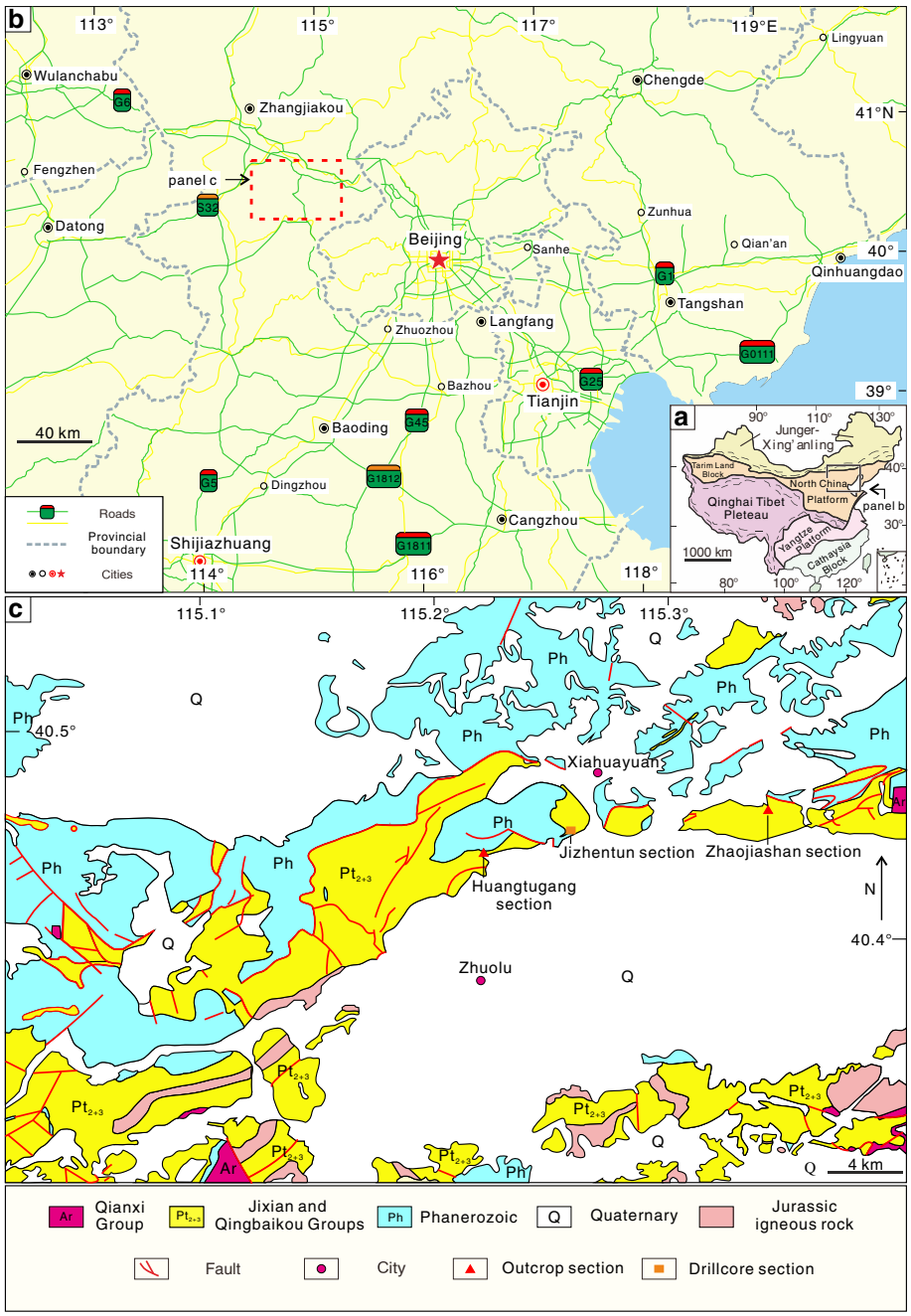

Fig. 1 **a** Major tectonic subdivisions of China (modified from Tang et al. 2017); the box showing the area illustrated in panel b; **b** Simplified map showing the location of the study area; **c** Simplified geological map of the study area (modified after the 1:200,000 Geological Map of China, The China Geological Survey 2013)

Jixian Group and the overlying Changlongshan Formation of Qingbaikou Group (Fig. 2). In general, the Xiamaling Formation was interpreted as deposition in an extensional setting (Zhang et al. 2009, 2012, 2017b; Tang et al. 2017, 2018). The duration of this formation is constrained between ~ 1.40 Ga and ~ 1.35 Ga according to the high-precision zircon/baddeleyite ages of 1384.4 ± 1.4 Ma and 1392.2 ± 1.0 Ma from its middle part (Zhang et al. 2015) and 1345 ± 12 Ma and 1353 ± 14 Ma from the diabase sills in its upper part (Zhang et al. 2009). The studied interval is located in middle part of the Member IV (Fig. 2) and can be approximately estimated as ~ 1.36 Ga in age. Palaeomagnetic study suggested that the North China Platform was most likely located in between 10°N and 30°N during the deposition of the Xiamaling Formation (Evans and Mitchell 2011; Zhang et al. 2012). Organic

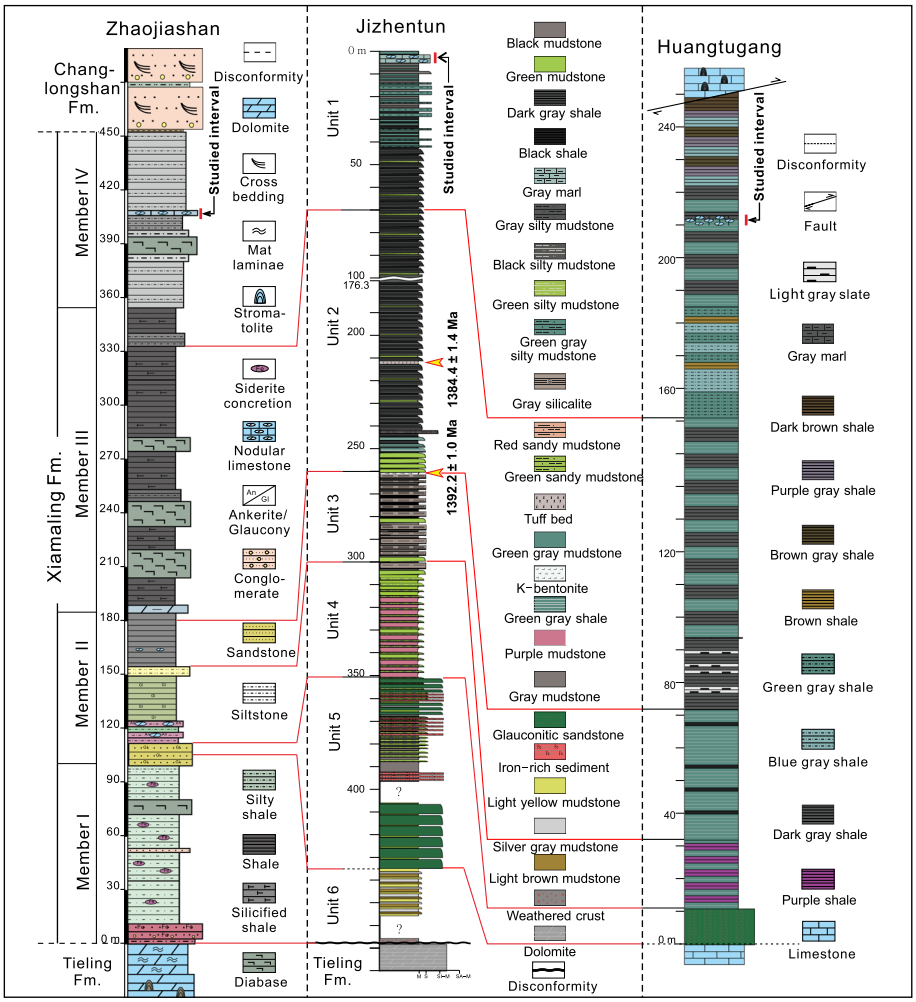

Fig. 2 Correlation of different subdivision schemes for the Xiamaling Formation in outcrop Zhaojiashan and Huangtugang sections and drillcore Jizhentun section used by different authors (Tang et al. 2017, 2018; Wang et al. 2017). The interval studied in this paper is in the Member IV or Unit 1

matter preserved in the Xiamaling Formation is ranked as immature to early thermal mature, with burial temperatures of ≤90 °C (Zhang et al. 2015; Tang et al. 2017, 2018).

In the study area, the Xiamaling Formation is dominated by dark siltstone and black shales, and can be subdivided into four members (Member I to IV) in an ascending order, which constitutes a large transgressive–regressive cycle with its largest depositional water-depth (below storm wave base) in the Member III (Fig. 2; Zhang et al. 2016; Tang et al. 2017, 2018). The lower to middle part of Member IV consists of alternating black and greenish shale, with a few limestone interbeds (Fig. 3a). The upper part of Member IV consists of a regressive succession from silty shale to yellowish siltstone in its upper portion, and is unconformably overlain by cross bedding-bearing medium to coarsely grained quartz sandstone of the Changlongshan Formation. The unconformity between the two formations was thought most likely to have resulted from the thermal uplifting prior to the onset of a large igneous province (e.g. Zhang et al. 2012, 2017b; Tang et al. 2018). To better elucidate recent advance and divergence in the study of the Xiamaling Formation, different subdivision schemes from the outcrop and drillcore successions for this formation are compared in Fig. 2 based on the lithology. As shown in the figure, the Member IV used in this study is roughly equivalent to the Unit 1 referred in Wang et al. (2017) and Zhang et al. (2017a).

Notably, there exists a ~6-m-thick carbonate concretion-bearing interval in the middle part of Member IV, which is widespread in the central North China Platform (Fig. 2), and is the focus of this study. Vertically, the abundance of concretions in the ~6-m-thick interval varies dramatically. They are sparse in some layers (Fig. 3a) but dense in other layers (Fig. 3b). The concretions are commonly ellipsoidal to tabular in shape, 3–20 cm in height and 5–40 cm in width, and are usually wrapped by bended thin layers of surrounding shale (Fig. 3).

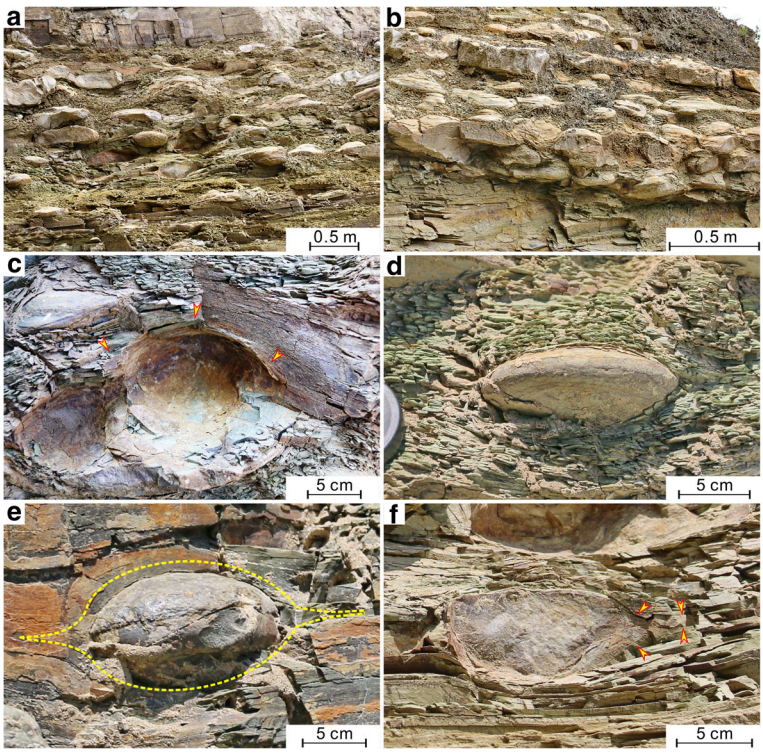

Fig. 3 Lithology and major sedimentary structures in the middle part of the Member IV of the Xiamaling Formation (Jizhentun section). **a** Sparsely distributed carbonate concretions in green-yellow silty shale; **b** Densely packed carbonate concretions in green-yellow silty shale; **c** Concretions wrapped by green silty shale laminae (arrows); **d** A concretion with sharp contact with the surrounding and lateral shale laminations; **e** and **f** Two concretions with lateral shale laminae (dash lines and arrows), and the laminae thickness in concretions is expanded by an order of magnitude relative to the laminae in adjacent shales

A deep-water setting below storm wave base has been suggested for most of the Member IV (Wang et al. 2017; Zhang et al. 2017a), except for a few intervals in its middle to upper part, in which hummocky and small-scale cross-bedding was sometimes observed, indicative of storm wave influence (Wang et al. 2017). The studied interval (marked with red bar in Fig. 2) consists mainly of green to gray silty shale with some centimeter-scale black shale interbeds and carbonate concretions (Fig. 3). Evidence of agitation from currents or waves rarely occur in this interval, likely indicating a depositional water-depth below but close to storm-wave base (> 100 m, Zhang et al. 2017a).

3 Materials and methods

Samples analyzed in this study were collected from the Member IV of the Xiamaling Formation, along road cuts at the Zhaojiashan (40°28′4.76″N, 115°24′5.74″E), Jizhentun (40°27′43.10″N, 115°16′29.48″E), and Huangtugang sections (40°27′8.62″N, 115°12′55.74″E), Hebei Province, North China (Fig. 1). Collected concretion samples were cut into chips and only central parts of the samples were used for geochemical analyses. Fresh sample chips were cleaned, dried, and then drilled for powders, avoiding weathered surfaces and recrystallized areas. Well-preserved samples were selected for microscope and SEM observations, and for chemical (EDS and trace element) analyses.

Macroscopic features were observed in the field and on polished slabs. Microfabrics were examined on thin sections with a Zeiss Stereo Discovery V20 microscope for large scope and a Zeiss Axio Scope A1 microscope for high magnification. Ultrastructures were investigated using a Zeiss Supra 55 field emission scanning electron microscope (FESEM) under 20 kV accelerating voltage with a working distance of ~ 15 mm, at the State Key Laboratory of Biogeology and Environmental Geology, China University of Geosciences (Beijing). Secondary electron imaging detector (SE2) was used to characterize topographic features, and an AsB detector was used to reveal compositional difference (backscattered electron, BSE, image). Samples were coated with 6-nm-thick platinum for electric conduction before analysis. A Gatan ChromaCL2 cathodoluminescence (CL) detector connected to the FESEM was used to obtain CL images under 8 kV accelerating voltage using ~ 30 min scanning time for each image.

Element concentrations of micron-sized spots were quantitatively analyzed by an Oxford X-act energy dispersive X-ray spectrometer (EDS) connected to the

FESEM, operated at 20 kV with a working distance of ~ 15 mm and a beam diameter of ~ 2 μm. Minerals as well as synthetic phases (MINM25–53) were used as reference standards. Duplicate analyses of individual points showed analytical error less than 2%.

For REE + Y analysis, ~ 50 mg of fine powder for each samples were weighed out and then rinsed with deionized water 4 times to remove clay minerals. For further minimizing the potential influence of terrigenous components on REE + Y, carbonate samples were dissolved using 5% acetic acid rather than other strong acids. Following the method described in Tang et al. (2016), the dissolved carbonate was carefully separated for REE analysis. The trace elements were measured in a PerkinElmer NexION 300Q Inductively Coupled Plasma Mass Spectrometry (ICP-MS) at National Research Center for Geoanalysis, Beijing. The accuracy of ICP-MS analyses is better than 10% (relative) for analyzed elements.

TOC contents of the shale samples were analyzed at the State Key Laboratory of Biogeology and Environmental Geology, China University of Geosciences (Beijing). For each, sample powder of 200 mg was treated with 5 M HCl for 48 h to remove any potential carbonate present. The carbonate-free residue was then rinsed by deionized water and centrifuged several times until *p*H test gives a neutral value. After drying, TOC was measured using an Elementar Vario Macro Cube element analyzer. The relative analytical uncertainty is < 0.5%.

For carbon isotope analysis, sample powders were drilled from polished slabs, avoiding weathered surfaces and recrystallized areas. Analyses were conducted at the State Key Laboratory of Biogeology and Environmental Geology, China University of Geosciences (Wuhan). About 150–400 μg of powder was placed in a 10 mL Na-glass vial, sealed with a butyl rubber septum, and reacted with 100% phosphoric acid at 72 °C after flushing with helium. The evolved CO_2 gas was analyzed for $\delta^{13}C$ and $\delta^{18}O$ using a MAT 253 mass-spectrometer coupled directly to a Finnigan GasBench II interface (Thermo Scientific). Isotopic values are reported as per mille relative to the Vienna Pee Dee belemnite (VPDB) standard. Analytical precision was better than ±0.1‰ for $\delta^{13}C$ and $\delta^{18}O$ based on replicate analyses of two laboratory standards (GBW 04416 and GBW 04417). The $\delta^{13}C$ and $\delta^{18}O$ of these two laboratory standards are + 1.61‰ and – 11.59‰, and – 6.06‰ and – 24.12‰, respectively.

4 Results

4.1 Features of carbonate concretions

The upper and lower contacts of concretions with host silty shale are sharp (Fig. 3c–f), while the lateral margins sometimes exhibit transition over a few centimeters (Fig. 3e and f). The lateral transition zone from silty shale to concretion carbonate is typically wedge-shaped, and tapers from a diffuse boundary at the concretion margin to the more compacted host shales (Fig. 3e and f). The concretion-hosting shales are commonly green in color, and mainly composed of glauconite and silty quartz with low TOC contents (Fig. 3). These shales were deposited in weakly oxygenated bottom seawater and experienced aerobic diagenesis processes (Zhang et al. 2017a).

Cross-sectioning reveals that the concretions are mainly composed of two parts: (1) replacive growth green-yellow part with lamination (called "R-horizons"), and (2) displacive growth off-white part with homogenous mass texture (called "D-horizons") (Fig. 4). In replacive growth, host sediments are incorporated into a concretionary body via extensive cementation of pore spaces, while displacive growth occurs where sedimentary beds are forced apart by growth of carbonate minerals (Gaines and Vorhies 2016). The laminae in R-horizons could be laterally extended into adjacent shales, while the D-horizons, vertically alternated with R-horizons, could not be extended into the adjacent shales, which is the simple marks for identification of R-horizons and D-horizons.

In the carbonate concretions of Xiamaling Formation, lamination fabrics commonly occupy a small portion (Fig. 4), and the laminae are likely extended from host silty shale but their thicknesses are expanded by an order (Fig. 3e and f). The texture and composition of these laminae are obviously different from the laminae in the host silty shale, and show the features of replacive growth. R-horizons are typically separated by portions of concretionary framework that grew displacively (Fig. 5a), and are mainly composed of clay minerals, fine detrital quartz and authigenic carbonate minerals (Fig. 5b). The clay mineral component is dominated by illite with minor chamosite. Authigenic apatite also occurs within R-horizons. In the R-horizons, SEM analysis reveals abundant "cardhouse" structures, which are randomly stacked clay minerals with voids reserved in them (Fig. 5c and d). Surrounding the "cardhouse" structures, there are no rigid grains such as detrital quartz to support the voids from being compacted. SEM analysis also reveals deflected clay mineral laminae around authigenic carbonate minerals (Fig. 5e). In contrast, in the host silty shale these phenomena are not seen (Fig. 5f–h). The host silty shale consists mainly of clay minerals (illite) and tiny quartz (Fig. 5f–h), with TOC content commonly less than < 0.2 wt% (0.12 ± 0.06 wt%, $n = 8$).

Intervals characterized by displacive growth constitute the dominant portion of the carbonate concretions of Xiamaling Formation, and were separated by R-horizons (Fig. 4). They are commonly several centimeters in thickness, but in the R-horizon dominated intervals some laterally continuous D-horizons are quite thin (< 1 mm) (Fig. 4c). D-horizons are composed dominantly of calcite with minor amount of authigenic quartz (Fig. 6a–f). Geodes, with diameter around 1 mm, are abundant in

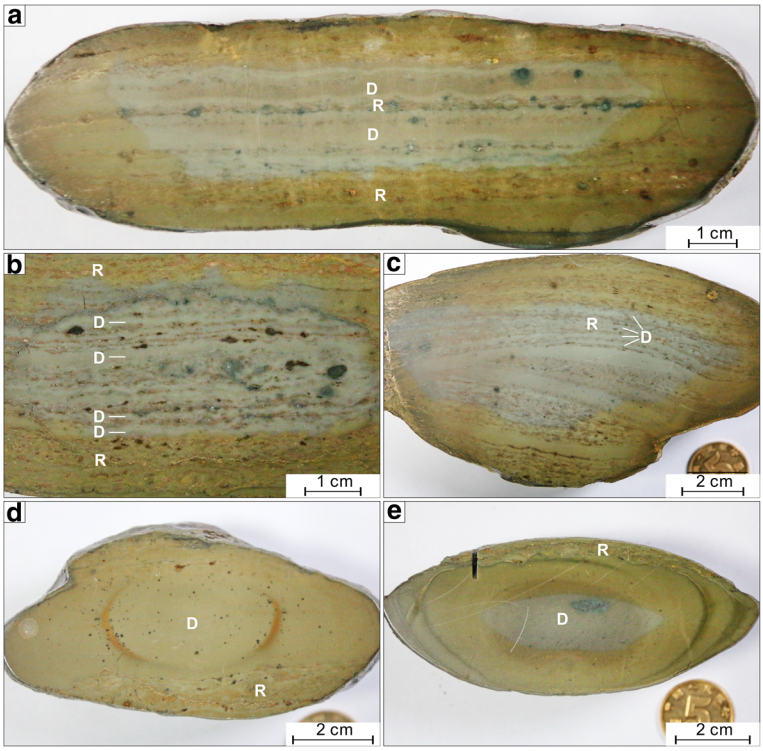

Fig. 4 Fabrics of the carbonate concretions of Xiamaling Formation. Displacive growth is marked with "D", while replacive growth marked with "R". **a** and **b** Polished concretions, showing offwhite zones of displacive growth, occurring within and adjacent to green-yellow zones of replaced mudstone that have been cemented and incorporated into the concretion fabric; **c** A concretion with curved lamination, showing that the displacive layer also occurred in a replacive layer concentrated zone; **d** and **e** Concretion with concentric ring structures. **a** and **d** were collected from Huangtugang section; the others were collected from Jizhentun section

the D-horizons. The calcite crystals away from the geodes are commonly small, < 20–100 μm in diameter (Fig. 6a), while they become large and rod-like in morphology (50 μm × 200 μm) close to or in the geodes (Fig. 6b–e). Light-microscope and BSE images reveal that the centers of some geodes were filled with siliciclastic chamosite, illite, and later diagenetic euhedral carbonate minerals that have dolomite nucleus and ankerite rim, and minor amount of pyrite grains (Fig. 6c and d). Sometimes, the calcite crystals are surrounded by clay minerals (Fig. 6f). In most of the samples, calcite in D-horizons exhibits dull orange or black color under CL (Fig. 6g and h). EDS analysis results confirm that the black area contains low concentrations of Mn and Fe, while the dull orange area has relatively high Mn and Fe concentrations.

4.2 Major elements

Light-microscope observation shows that the carbonate concretions analyzed in this study have not suffered intensive recrystallization, with the component microspar commonly less than 50 μm (Fig. 6). EDS analysis of 93 points reveal that the dolomitization is rather weak, with MgO content commonly less than 1 wt% and Mg/Ca molar ratio lower than 0.04 (Additional file 1: Table S1). As shown in Fig. 7a–e, calcite crystals commonly have an irregular nucleus–rim structure, with low Mn–Fe contents in the nuclei, and relatively high Mn–Fe contents in the rims. Mn and Fe contents in the nuclei are commonly 0.03 ± 0.03 wt% and 0.06 ± 0.05 wt%, respectively; while those in the rims are 0.42 ± 0.18 wt% and 0.44 ± 0.23 wt%, respectively (Additional file 1: Table S1). In addition, Mn/Fe ratios in the rims (3.3) are higher than those seen in the carbonates formed in ferruginous (0.10) and oxic environments (0.14), and also higher than those formed in a manganese-rich environment (0.39, Fig. 7f; Tostevin et al. 2016).

4.3 Stable isotope geochemistry

As shown in Table 1 and illustrated in Fig. 7g, selected 21 carbonate concretions show $\delta^{13}C_{carb}$ values around 0.4‰ (− 1.7‰ to + 1.5‰), and $\delta^{18}O_{carb}$ values around − 7.5‰ (− 10‰ to − 4.8‰). All of the $\delta^{13}C_{carb}$ values fall into the typical range of "Boring Billion" (Brasier and Lindsay 1998) carbonate values (e.g. Guo et al. 2013).

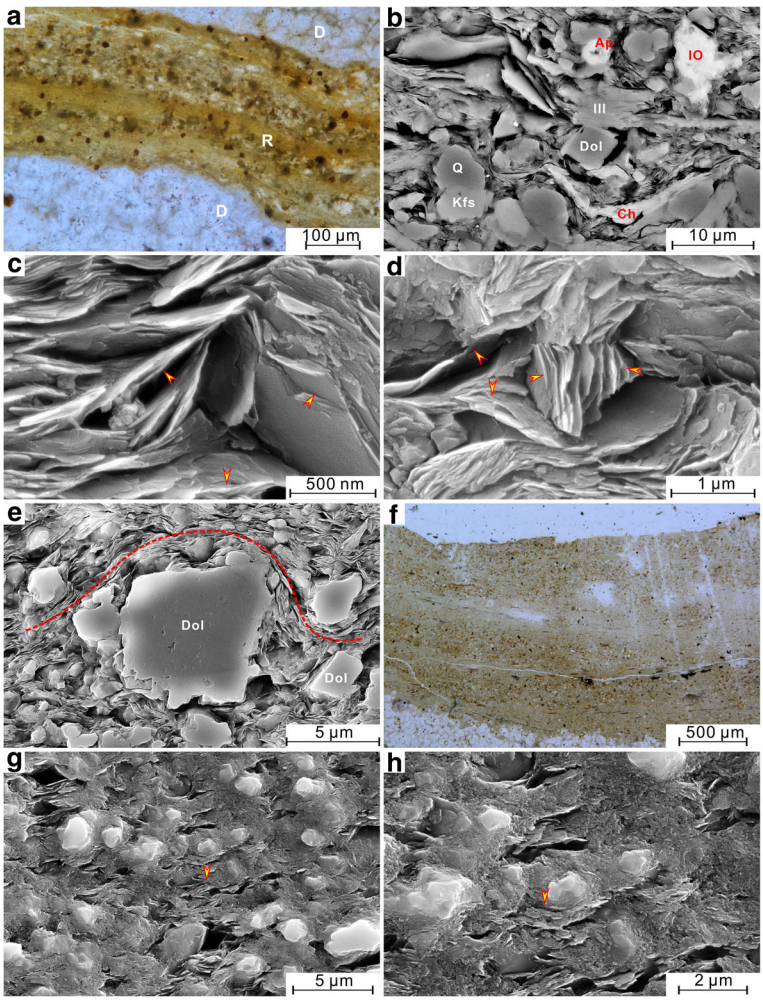

Fig. 5 Composition and texture of replacive layers in the carbonate concretions of Xiamaling Formation (Jizhentun section). **a** A green-yellow replacive layer (marked by R) interbedded in displacive layers (marked by D); **b** A BSE image showing that the replacive layer is composed of siliciclastic illite (Ill), chamosite (Ch), quartz (Q), K-feldspar (Kfs) and iron oxides (IO), and authigenic dolomite (Dol) and apatite (Ap); **c** and **d** "Cardhouse" structures (arrows) in the replacive layer; **e** SEM image of replaced mudstone horizon in a concretion, showing laminar clay minerals bended around an authigenic dolomite grain (dash line); **f** Green-yellow silty shale matrix adjacent to a concretion; **g** SEM image of panel **f** showing horizontal clay lamination (arrow); **h** SEM image with high magnification, showing horizontally distributed laminar clay minerals (arrow)

4.4 REE of carbonates

The REEs of calcites from 9 carbonate concretions of Xiamaling Formation (Huangtugang section) are listed in Table 2 and shown in Fig. 7h. Calcite samples digested by 5% acetic acid show REE concentrations of 35–133 μg/g. PAAS (Post-Archean Australian Shale)-normalized REE distribution patterns (REE_{SN}) of the calcites show prominent positive Ce anomalies (calculated as $Ce/Ce^* = Ce_{SN}/(Pr_{SN}^2/Nd_{SN})$) and moderate enrichment of middle REE (MREE) (Table 2, Fig. 7h). The average Y/Ho ratio in the studied samples is about 31, close to the PAAS composite ratio (~ 27, McLennan 1989). All the tested samples show no obvious Eu anomalies (1.03–1.12, calculated as $Eu/Eu^* = Eu_{SN}/(0.66Sm_{SN} + 0.33Tb_{SN})$).

5 Discussion

5.1 Evidence for rapid growth of concretions

The growth of carbonate concretions in dark shale is most commonly estimated to take place over a time-range of 10^3 to > 10^6 years (Sellés-Martínez 1996). For prolonged growth, zoned crystals (Raiswell 1988; Mozley 1989; Raiswell and Fisher 2000) and multiple generations of cements with distinct chemical and isotopic properties are commonly present (e.g. Hendry et al. 2006; Dale et al. 2014; Loyd et al. 2014). For rapid growth, the morphology of soft-bodied fossils could be preserved (e.g. Huggett et al. 2000; Feldmann et al. 2012; McCoy 2014), primary depositional fabrics would be remained, and specific fabrics indicative of pore-filling cementation prior to burial compaction would be formed (e.g. Raiswell and Fisher 2000; Day-Stirrat et al. 2008).

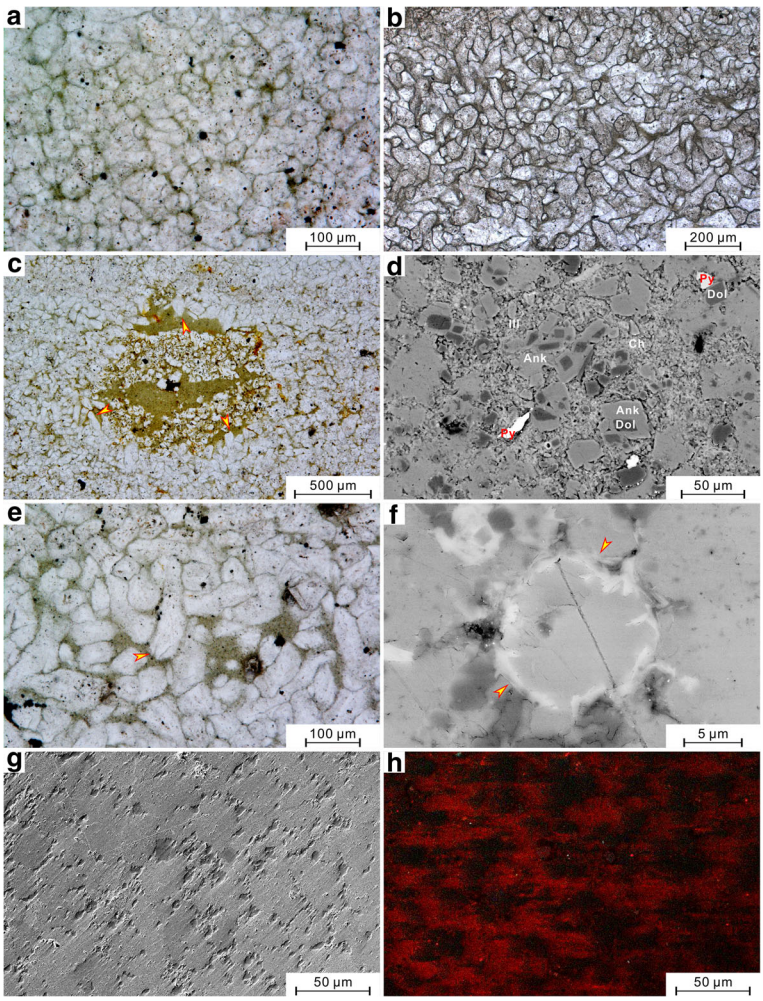

Fig. 6 Composition and texture of displacive layers in carbonate concretions of Xiamaling Formation (Jizhentun section). **a** Small sized calcite crystals (< 20–100 μm) in a displacive layer; **b** Calcite crystals with rod-like morphology, with their width and length up to ~ 50 μm and ~ 200 μm, respectively; **c** A calcite geode, showing that the rod-like minerals have their long axis toward the center of the geode (arrows), and the geode center is filled with green-yellow clay and later diagenetic subhedral to euhedral carbonate minerals; **d** BSE image of the geode center in panel c, showing that the clay minerals are mainly of chamosite (Ch) with minor illite (Ill); the carbonate minerals have dolomite (Dol) nuclei and ankerites (Ank) rim; with some pyrite (Py) grains; **e** A calcite geode, showing that the rod-like minerals in the geode have higher length-width ratio and larger size (arrow) than those of surrounding minerals; **f** BSE image showing a calcite crystal surrounded by clay minerals (arrow); **g** and **h** SEM image and the CL image of the same area, showing that some areas display no luminescence, while the others show weak orange luminescence

In our study, a number of lines of evidence shows that the carbonate concretions from the Member IV of Xiamaling Formation grew rapidly during early diagenesis and were formed prior to significant compaction of clay minerals. The evidence comprises the deflected laminae wrapping the concretions (Fig. 3c–f), bending clay-rich laminae surrounding authigenic carbonate minerals (Fig. 5e) and well preserved "cardhouse" structures in R-horizons (Fig. 5c and d), and calcite geodes in D-horizons (Fig. 6c–e). Dolomite crystals surrounded by curved laminae in R-horizons (Fig. 5e) reveal that the carbonate matrix grew freely within the mudstone beds, pushing clay grains aside and disrupting the primary depositional fabric (Gaines and Vorhies 2016). The presence of "cardhouse" structures in concretions (Fig. 5c and d) has been interpreted as a primary depositional feature, and their preservation could be ascribed to passive porefilling carbonate growth prior to the significant compaction of clays (e.g. Day-Stirrat et al. 2008; Dong et al. 2008). The calcite crystals are commonly small, < 100 μm in size, but in geodes they become larger and rod-shape in morphology (length and width up to 50 μm and 200 μm, respectively; Fig. 6). This likely implies that parts of the rigid framework of the concretions were formed rather rapidly and considerably earlier than the significant compaction of host sediments. Therefore, plentiful spaces

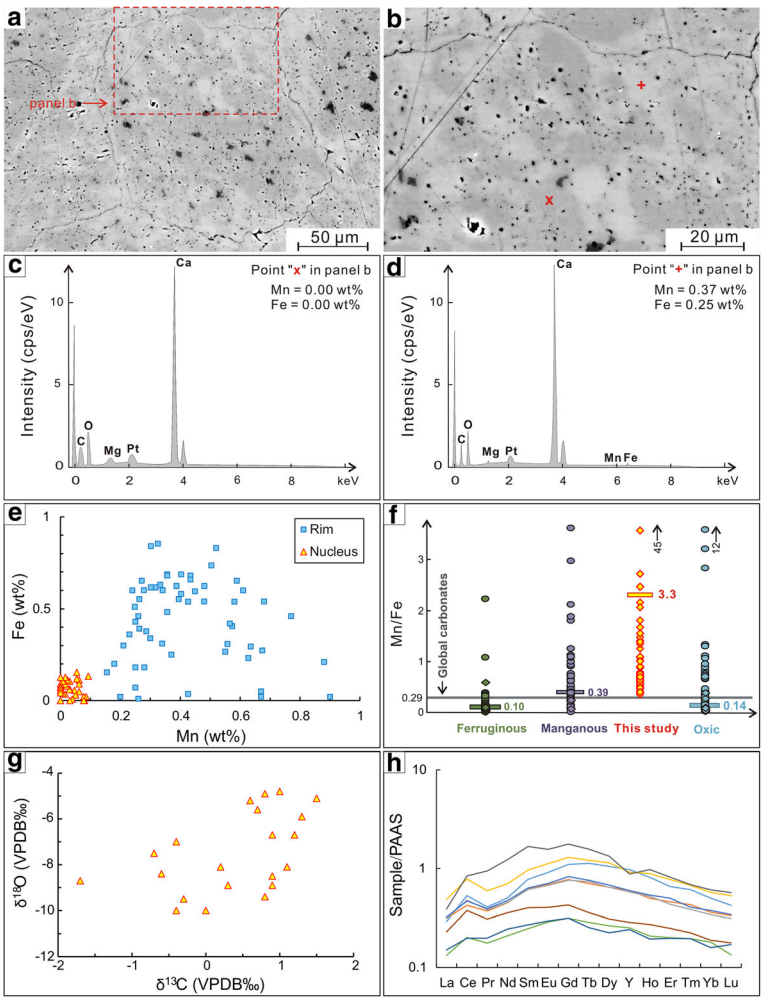

Fig. 7 BSE images and chemistry of calcites in the carbonate concretions of Xiamaling Formation. **a** and **b** BSE images, showing a calcite crystal with dark nucleus (low Mn–Fe contents) and light rim (high Mn–Fe contents) (Zhaojiashan section); **c** and **d** EDS spectrums showing that the Mn–Fe contents of the nucleus are lower than the detection limits of EDS, while the rim has higher Mn–Fe contents; **e** A cross plot showing that the nuclei of calcite crystals have low Mn and Fe concentrations, while the rims have high Mn and Fe concentrations; **f** Average Mn/Fe ratios under different redox conditions. Mn/Fe ratios are enriched in our samples compared with those of average global carbonate (0.29; Turekian and Wedepohl 1961) and of manganous samples (Tostevin et al. 2016). Bars represent median values; arrows indicate samples with exceptionally high Mn/Fe ratios that lie above the limit of the Y axis; **g** A cross plot of $\delta^{13}C$ vs. $\delta^{18}O$; **h** REE patterns of the carbonate concretions, showing prominent positive Ce anomalies and slight enrichment of MREE

were retained in the cavities for large and elongated mineral growth (Raiswell and Fisher 2000).

5.2 Growth mechanisms of concretions

The growth of carbonate concretions in mudrocks commonly results from carbonate supersaturation in porewaters, which is typically caused by high alkalinity generated by microbial respiration of organic matter in suboxic to anoxic sediments (e.g. Sellés-Martínez 1996; Loyd et al. 2012). Consequently, $\delta^{13}C$ values of concretion carbonates are often used as fingerprints for specific microbial pathways that may have triggered and maintained concretion growth (e.g. Fisher et al. 1998; Raiswell and Fisher 2000, 2004; Raiswell et al. 2002; Loyd et al. 2012; Dale et al. 2014; Gaines and Vorhies 2016). Isotopic studies of mudrock-hosted concretions from rock record show that they are commonly characterized by conspicuously depleted and variable $\delta^{13}C$ signatures that can reach low values of − 10‰ (e.g. Mozley and Burns 1993; Raiswell and Fisher 2000). However, analysis of 21 carbonate concretions from the Member IV of Xiamaling Formation (Zhaojiashan and Huangtugang sections) shows different results (Table 1, Fig. 7g).

The $\delta^{13}C$ values of analyzed samples range from − 1.7‰ to + 1.5‰, and are close to or slightly lower than the value of contemporaneous seawater (Guo et al. 2013). These data suggest a significantly less contribution of organic matter to the growth of carbonate concretions of Xiamaling Formation than that of typical

Table 1 Carbon and oxygen isotopes of carbonate concretions from the Member IV of Xiamaling Formation (Zhaojiashan and Huangtugang sections)

Serial No.	Sample ID	Thickness (m)	Section	$\delta^{13}C$ (VPDB‰)	$\delta^{18}O$ (VPDB‰)
No. 01	ZJS-24-3-1a	1.2	ZJS	0.8	−9.4
No. 02	ZJS-24-3-1b	1.2	ZJS	0.0	−10.0
No. 03	ZJS-24-3-1c	1.2	ZJS	1.3	−5.9
No. 04	ZJS-24-7-1a	2.3	ZJS	0.9	−8.9
No. 05	ZJS-24-7-1b	2.3	ZJS	0.9	−6.7
No. 06	ZJS-24-9-1a	2.5	ZJS	1.5	−5.1
No. 07	ZJS-24-9-1b	2.5	ZJS	1.2	−6.7
No. 08	ZJS-24-11-1	2.6	ZJS	0.9	−8.5
No. 09	ZJS-24-15-1	3.1	ZJS	−0.3	−9.5
No. 10	ZJS-24-15-2	3.1	ZJS	0.7	−5.6
No. 11	ZJS-24-19-1	3.7	ZJS	0.2	−8.1
No. 12	ZJS-24-21-1a	3.8	ZJS	−0.4	−10.0
No. 13	ZJS-24-23-1	4.4	ZJS	0.3	−8.9
No. 14	ZJS-24-25-1	4.5	ZJS	1.1	−8.1
No. 15	ZJS-24-J	5.6	ZJS	1.0	−4.8
No. 16	1704HTG-3	1.5	HTG	−0.7	−7.5
No. 17	1704HTG-4	2	HTG	−0.6	−8.4
No. 18	1704HTG-6	3	HTG	0.6	−5.2
No. 19	1704HTG-8	4	HTG	−0.4	−7.0
No. 20	1704HTG-9	4.5	HTG	−1.7	−8.7
No. 21	1704HTG-10	5	HTG	0.8	−4.9
	Min			−1.7	−10.0
	Max			1.5	−4.8
	Average			0.4	−7.5

Note: *ZJS* Zhaojiashan, *HTG* Huangtugang

carbonate concretions formed in organic-rich mudstones (e.g. Gaines and Vorhies 2016), and indicate that AOM and methanogenesis should not be the dominated processes for the formation of these concretions. On the contrary, the growth of the carbonate concretions from the Member IV of Xiamaling Formation appears to have been significantly influenced by overlying seawater chemistry. The inorganic pool of bicarbonate in porewaters should be open to re-supplement by diffusion to account for the large masses of carbonate concretions of Xiamaling Formation. This is different from most carbonate concretions in the marine records that commonly resulted from the development of microenvironments in relative isolation from seawater. The calcite was likely precipitated close to the seawater/sediment interface, where the majority of dissolved inorganic carbon (DIC) was largely sourced from overlying seawater with elevated DIC reservoir. Even so, the primary carbonates were not directly formed on the seafloor, suggesting that the bicarbonate from degraded organic matter and the nucleation sites provided by degraded organic matters may have played significant roles in triggering the initial carbonate precipitation as well. Comparable cases are rare in Phanerozoic marine sediments, but occur in the carbonate concretions from the Cambrian Wheeler Formation (Utah, USA), when the seawater has an elevated DIC reservoir (Gaines and Vorhies 2016).

The mineralogy of the carbonate concretions of Xiamaling Formation and elemental compositions of calcites within the concretions may provide further information concerning the potential physical and biogeochemical processes during early diagenesis. The D-horizons of concretions commonly have homogeneous textures, with almost all calcites having nucleus–rim structures, likely indicating that the concretions mainly grew pervasively rather than concentrically (Raiswell and Fisher 2000). Although some pyrite grains sometimes occur in the center of some geodes, which grew later than that of the main bodies of the concretions, the rare presence of pyrite in the main bodies of the concretions likely indicate that the BSR was not the dominated process for the formation of these concretions. The relatively high Mn–Fe contents and high Mn/

Table 2 REE concentrations of carbonate concretions from the Member IV of Xiamaling Formation (Huangtugang section)

Sample ID	La	Ce	Pr	Nd	Sm	Eu	Gd	Tb	Dy	Y	Ho	Er	Tm	Yb	Lu	Ce/Ce*	Eu/Eu*	Y/Ho	Pr_{SN}/Yb_{SN}
1704HTG-3	11.100	42.500	3.620	16.100	4.340	1.006	5.168	0.869	4.620	26.300	0.813	1.900	0.244	1.400	0.182	1.62	1.03	32.3	0.81
1704HTG-4	12.000	33.900	3.300	14.400	3.480	0.756	3.635	0.543	2.840	16.200	0.499	1.330	0.172	1.010	0.143	1.39	1.06	32.5	1.03
1704HTG-6	11.900	38.200	3.400	14.500	3.430	0.741	3.576	0.567	2.840	15.600	0.523	1.260	0.154	0.955	0.134	1.48	1.03	29.8	1.12
1704HTG-8	18.500	62.500	5.300	22.400	5.390	1.233	6.093	0.932	5.020	24.800	0.887	2.240	0.270	1.600	0.228	1.54	1.07	28.0	1.04
1704HTG-9	12.300	37.500	3.490	15.100	3.550	0.777	3.884	0.584	2.990	16.100	0.537	1.450	0.162	1.050	0.147	1.44	1.05	30.0	1.05
1704HTG-10	5.060	16.100	1.570	6.690	1.380	0.317	1.479	0.220	1.160	6.780	0.208	0.581	0.078	0.505	0.058	1.35	1.11	32.6	0.98
1704HTG-12	5.760	15.800	1.760	7.830	1.510	0.325	1.479	0.195	0.988	6.530	0.194	0.572	0.078	0.445	0.073	1.24	1.12	33.7	1.24
1704HTG-14	8.770	30.000	2.740	11.400	2.240	0.444	2.006	0.275	1.360	7.710	0.272	0.721	0.090	0.528	0.076	1.41	1.05	28.3	1.63
Min	5.060	15.800	1.570	6.690	1.380	0.317	1.479	0.195	0.988	6.530	0.194	0.572	0.078	0.445	0.058	1.24	1.03	28.0	0.81
Max	18.500	62.500	5.300	22.400	5.390	1.233	6.093	0.932	5.020	26.300	0.887	2.240	0.270	1.600	0.228	1.62	1.12	33.7	1.63
Average	10.674	34.563	3.148	13.553	3.165	0.700	3.415	0.523	2.727	15.003	0.492	1.257	0.156	0.937	0.130	1.43	1.06	30.9	1.11

Note: the unit of REE + Y concentration is ug/g

Fe ratios in the rims of calcite crystals (Fig. 7a–f) likely indicate that the rims were formed in a Mn reduction zone (Curtis et al. 1986; Tostevin et al. 2016). As the Mn–Fe contents in the nuclei are lower than those in the rims and are black in color under CL, we could further deduce that the calcite precipitation was initiated in the nitrate reduction zone above the Mn reduction zones (Fig. 8). The growth process of the concretion is probably as follows. In the nitrate reduction zone, nucleation and the initial precipitation of calcite in the

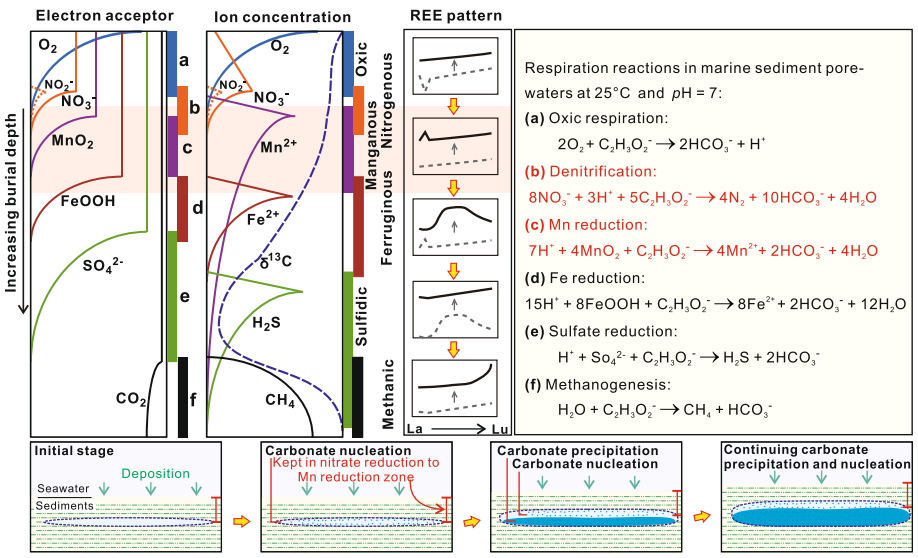

Fig. 8 Schematic illustration of diagenetic environment with redox zones in marine sediment porewaters (adapted from Canfield and Thamdrup 2009), modeled aqueous REE patterns in sediment porewaters ranging from the oxic to methanic zones (adapted from Haley et al. 2004 and Kim et al. 2012), and possible growth model for the carbonate concretions of Xiamaling Formation. In different redox zones, different electron acceptors, including O_2, NO_2^-, NO_3^-, MnO_2, FeOOH, SO_4^{2-} and CO_2 are predominated, and different REE patterns of porewater appear with positive Ce anomaly in Mn reduction zone and enrichment of MREE in Fe reduction zone. The formation of carbonate concretions of Xiamaling Formation mainly occurred in the Mn reduction zone, and probably also extended to the upper nitrate and lower Fe reduction zones

concretions happened, therefore the Mn–Fe-poor nuclei were formed. Subsequent growth likely occurred in the Mn reduction zone with slightly increased burial depth, therefore the high Mn–Fe rims were formed. In fact, both nitrate reduction ($5C_2H_3O_2^- + 8NO_3^- + 3H^+ \rightarrow 4N_2 + 10HCO_3^- + 4H_2O$) and manganese reduction ($C_2H_3O_2^- + 4MnO_2 + 7H^+ \rightarrow 2HCO_3^- + 4Mn^{2+} + 4H_2O$) could facilitate the precipitation of calcite during early diagenesis by increasing environmental alkalinity and *p*H (Fig. 8; e.g. Loyd et al. 2012).

The REE + Y patterns of the carbonate concretions of Xiamaling Formation provide further support for their early diagenetic origin mainly through Mn reduction process. In an oxic water column, Ce, Ho and MREEs are preferably removed by Mn–Fe oxyhydroxides (German and Elderfield 1990; Byrne and Sholkovitz 1996; Bau and Dulski 1999; Haley et al. 2004; Gutjahr et al. 2007; Planavsky et al. 2010). The Ce, Ho and MREEs absorbed or scavenged to Mn–Fe oxyhydroxides would be expected to be released below the Mn–Fe redoxcline in the water column or just below the seawater/sediment interface, resulting in high Ce, Ho, and MREE concentrations and therefore positive Ce anomaly, low Y/Ho ratio and MREE enrichment in sediments/cements (e.g. de Baar et al. 1988; German et al. 1991; Bau et al. 1997; De Carlo and Green 2002; Planavsky et al. 2010; Tostevin et al. 2016). Thus, the positive Ce anomalies and low Y/Ho ratios in the carbonate concretions of Xiamaling Formation (Huangtugang section) (Fig. 7h; Table 2) also support the idea that calcite precipitation was facilitated by Mn reduction in the sediments, while the slight MREE enrichment indicates a partial contribution from iron reduction (Fig. 8; Haley et al. 2004).

Based on the integration of petrographic, mineralogical, carbon isotopic and elemental geochemical data, the carbonate concretions of Xiamaling Formation are best interpreted as early diagenetic products that may have been formed largely in nitrate to Mn reduction zones, with some of them also extending into the iron reduction zone below the Mn reduction zone via displacive growth (Fig. 8). The dark nuclei of calcite crystals in the BSE image (low Mn and Fe; black under CL) were possibly formed in the zone of nitrate reduction, while the following growth of light outer rims of calcite crystals (high Mn and Fe; dull orange under CL) were likely formed during Mn reduction. Considering that the Mn reduction zone is commonly thin (Thamdrup et al. 1994; Haley et al. 2004; Meyer et al. 2005) but the carbonate concretions of Xiamaling Formation are thick, we deduced that the concretions grew vertically with the reaction front likely remaining in the nitrate and Mn reduction zone during the whole forming process of the carbonate concretions of Xiamaling Formation, through keeping the upward growth rate close to that of siliciclastic deposition (Fig. 8). Nitrate and Mn reductions were the predominant processes of initiating the precipitation, but it was the seawater with high concentration of bicarbonate that facilitated the subsequently persistent carbonate precipitation.

5.3 Palaeoenvironmental implications

The carbonate concretions were mainly induced by Mn reduction in host silty shale. Their development in the Member IV of the Xiamaling Formation likely indicates that high Mn-hydroxide content and an expanded Mn reduction zone existed in the sediments. In modern oxygenated oceans, the average thickness of the Mn reduction zone is only several centimeters (Thamdrup et al. 1994; Haley et al. 2004; Meyer et al. 2005) and owing to the less prominent Mn reduction process, no positive Ce anomalies exist in this zone (Haley et al. 2004). As the elevated *p*H and HCO_3^- provided by the Mn reduction are limited in the thin Mn reduction zone, thus documented examples for carbonate concretions formed in the Mn reduction zone are rare. Instead, BSR, AOM, and methanogenesis were more often identified and suggested as the predominant processes for carbonate concretion formation (Curtis et al. 1986; Raiswell and Fisher 2000; Hendry et al. 2006; Loyd et al. 2012; Dong et al. 2013).

The biogeochemical processes recorded by early diagenetic concretions in sediments, in turn, have the potential to reflect the seawater chemistry indirectly. The presence of an expended Mn reduction zone in the sediments likely indicated that the Mn redox cycling in the overlying seawater was abnormally active, and there possibly existed a manganous zone in the deep seawater and a Mn-redoxcline in the shallow seawater. Around the Mn-redoxcline, Mn^{2+} was rapidly oxidized to Mn-hydroxides and then precipitated on the seafloor providing abundant oxidants for diagenetic Mn reduction. The existence of a manganous zone in the seawater column was commonly used as a signature for oxygenated shallow seawater with oxygen concentration higher than 10 μM (e.g. Tostevin et al. 2016). This is mainly based on the observation that in modern oceans active Mn redox cycling could only occur when the oxygen concentration is at least higher than 10 μM (e.g. Trefry et al. 1984; Saager et al. 1989; German and Elderfield 1990; Johnson et al. 1992). This oxygen concentration is obviously higher than that estimated for the mid-Proterozoic based on Cr isotopes recorded by ironstones (< 0.1% PAL; Planavsky et al. 2014) and shales (< 1% PAL; Cole et al. 2016), but in good consistence with the suggestion that there existed an oxygenation event at ~ 1.4 Ga with atmospheric oxygen concentration > 4%–8% PAL (Zhang et al. 2016, 2017a). The weakly oxygenated seawater has also been proved by aerobic diagenetic processes identified in concretion-hosting green silty shales (Zhang et al. 2017a).

The development of carbonate concretions largely in the Mn reduction zone and their seawater-like carbon isotope compositions provide evidence that the seawater had a high concentration of bicarbonate facilitating the concretion formation. This deduction is in good consistence with the frequent occurrence of seafloor precipitations (e.g. Tang et al. 2015) and the overall less variable carbonate carbon isotopes during the Mesoproterozoic (Bartley and Kah 2004; Guo et al. 2013). If this deduction is the case, many similar concretions formed in nitrate and Mn reduction zones with seawater-like carbon isotope composition should exist in the Mesoproterozoic strata and further studies are required to test this explanation.

6 Conclusions

1) Carbonate concretions are widespread in the organic-poor green silty shales from the Member IV of Xiamaling Formation (1.40–1.35 Ga) in the North China Platform. They are composed mainly of displacive growth horizons with a small portion of replacive growth horizons.
2) The deformed laminae surrounding the concretions, "cardhouse" structures in R-horizons and the geodes in D-horizons indicate that they are of rapid early diagenetic origin before the significant compaction of clay minerals.
3) Many lines of mineralogical and geochemical evidence, including the seawater-like carbon isotope composition, rare occurrence of pyrite grains, nucleus–rim structure of calcites with low Mn–Fe nuclei and high Mn–Fe rims, and positively Ce anomalies of calcites, synthetically are evidence that the carbonate concretions of Xiamaling Formation were formed largely in nitrate to Mn reduction zones during early diagenesis just below the seawater/sediment interface, where high HCO_3^- seawater could freely exchange with porewater in sediments.
4) The Mn reduction zone was likely more expanded in the Mesoproterozoic Xiamaling sediments than that in the Phanerozoic, thus we interpret that Mn redox cycling in the overlying seawater was active, invoking existence of a manganous zone and moderately oxygenated seawater conditions. This is consistent with the suggestion that the atmospheric oxygen level was likely higher than 4% PAL during the deposition of the Member IV of Xiamaling Formation.

7 Additional file

Additional file 1: Table S1. EDS analysis results of carbonate concretions from the Member IV of Xiamaling Formation. (XLS 45 kb)

Abbreviations

AOM: Anoxic oxidation of methane; BSE: Backscattered electron; BSR: Bacterial sulfate reduction; CL: Cathodoluminescence; DIC: Dissolved inorganic carbon; DIR: Dissimilatory iron reduction; EDS: Energy dispersive spectrometry; FESEM: Field emission scanning electron microscope; ICP-MS: Inductively Coupled Plasma Mass Spectrometry; MREE: Middle rare earth element; PAAS: Post-Archean Australian Shale; PAL: Present atmospheric level; REE: Rare earth element; SEM: Scanning electron microscope; TOC: Total organic carbon; VPDB: Vienna Pee Dee belemnite

Acknowledgements

The study was supported by the National Natural Science Foundation of China (No. 41672336), and by the Fundamental Research Funds for the Central Universities (No. 2652018005 and 2652017050). Thanks are given to Hao-Ming Wei, Zhi-Peng Wang and Tong Wu for their assistance in field work.

Authors' contributions

DJT designed the study. DJT, AQL, MHS and YL collected the samples. AQL, LMZ, MHS, YL and HYS carried out the experiment. AQL and DJT wrote the manuscript, and XYS and XQZ helped modify the manuscript. All authors read and approved the final manuscript.

Competing interests

The authors declare that they have no competing interests.

Publisher's Note

Author details

[1]State Key Laboratory of Biogeology and Environmental Geology, China University of Geosciences (Beijing), Beijing 100083, China. [2]Institute of Earth Sciences, China University of Geosciences (Beijing), Beijing 100083, China. [3]School of Earth Sciences and Resources, China University of Geosciences (Beijing), Beijing 100083, China. [4]National Research Center for Geoanalysis, Beijing 100037, China. [5]Key Lab of Petroleum Resources Research, Institute of Geology and Geophysics, Chinese Academy of Sciences, Beijing 100029, China. [6]State Key Laboratory of Biogeology and Environmental Geology, China University of Geosciences (Wuhan), Wuhan 430074, China.

Received: 23 January 2019 Accepted: 23 April 2019
Published online: 16 May 2019

References

Bartley, J.K., and L.C. Kah. 2004. Marine carbon reservoir, C_{org}-C_{carb} coupling, and the evolution of the Proterozoic carbon cycle. *Geology* 32 (2): 129–132.

Bau, M., and P. Dulski. 1999. Comparing yttrium and rare earths in hydrothermal fluids from the Mid-Atlantic Ridge: Implications for Y and REE behaviour during near-vent mixing and for the Y/Ho ratio of Proterozoic seawater. *Chemical Geology* 155 (1–2): 77–90.

Bau, M., P. Möller, and P. Dulski. 1997. Yttrium and lanthanides in eastern Mediterranean seawater and their fractionation during redox-cycling. *Marine Chemistry* 56 (1): 123–131.

Baumgartner, L.K., R.P. Reid, C. Dupraz, A.W. Decho, D.H. Buckley, J.R. Spear, K.M. Przekop, and P.T. Visscher. 2006. Sulfate reducing bacteria in microbial mats: Changing paradigms, new discoveries. *Sedimentary Geology* 185 (3–4): 131–145.

Brasier, M.D., and J.F. Lindsay. 1998. A billion years of environmental stability and the emergence of eukaryotes: New data from northern Australia. *Geology* 26 (6): 555–558.

Byrne, R.H., and E.R. Sholkovitz. 1996. Chapter 158 Marine chemistry and geochemistry of the lanthanides. In *Handbook on the Physics and Chemistry of Rare Earths 23*, 497–593.

Canfield, D.E., B.B. Jørgensen, H. Fossing, R. Glud, J. Gundersen, N.B. Ramsing, B. Thamdrup, J.W. Hansen, L.P. Nielsen, and P.O.J. Hall. 1993. Pathways of organic carbon oxidation in three continental margin sediments. *Marine Geology* 113 (1–2): 27–40.

Canfield, D.E., and B. Thamdrup. 2009. Towards a consistent classification scheme for geochemical environments, or, why we wish the term 'suboxic' would go away. *Geobiology* 7 (4): 385–392.

Cole, D.B., C.T. Reinhard, X.L. Wang, B. Gueguen, G.P. Halverson, T. Gibson, M. S.W. Hodgskiss, N.R. McKenzie, T.W. Lyons, and N.J. Planavsky. 2016. A shale-hosted Cr isotope record of low atmospheric oxygen during the Proterozoic. *Geology* 44 (7): 555–558. https://doi.org/10.1130/G37787.1.

Curtis, C.D., M.L. Coleman, and L.G. Love. 1986. Pore water evolution during sediment burial from isotopic and mineral chemistry of calcite, dolomite and siderite concretions. *Geochimica et Cosmochimica Acta* 50 (10): 2321–2334.

Dale, A., C.M. John, P.S. Mozley, P.C. Smalley, and A.H. Muggeridge. 2014. Time-capsule concretions: Unlocking burial diagenetic processes in the Mancos Shale using carbonate clumped isotopes. *Earth and Planetary Science Letters* 394: 30–37.

Day-Stirrat, R.J., R.G. Loucks, K.L. Milliken, S. Hillier, and B.A. van der Pluijm. 2008. Phyllosilicate orientation demonstrates early timing of compactional stabilization in calcite-cemented concretions in the Barnett Shale (Late Mississippian), Fort Worth Basin, Texas (USA). *Sedimentary Geology* 208 (1–2): 27–35.

de Baar, H.J.W., C.R. German, H. Elderfield, and P. van Gaans. 1988. Rare earth element distributions in anoxic waters of the Cariaco Trench. *Geochimica et Cosmochimica Acta* 52 (5): 1203–1219.

De Carlo, E.H., and W.J. Green. 2002. Rare earth elements in the water column of Lake Vanda, McMurdo Dry Valleys, Antarctica. *Geochimica et Cosmochimica Acta* 66 (8): 1323–1333.

Dong, J., S.H. Zhang, G.Q. Jiang, H.Y. Li, and R. Gao. 2013. Greigite from carbonate concretions of the Ediacaran Doushantuo Formation in South China and its environmental implications. *Precambrian Research* 225: 77–85.

Dong, J., S.H. Zhang, G.Q. Jiang, Q.L. Zhao, H.Y. Li, X.Y. Shi, and J.L. Liu. 2008. Early diagenetic growth of carbonate concretions in the upper Doushantuo formation in South China and their significance for the assessment of hydrocarbon source rock. *Science in China Series D: Earth Sciences* 51 (9): 1330–1339.

Evans, D.A.D., and R.N. Mitchell. 2011. Assembly and breakup of the core of Paleoproterozoic–Mesoproterozoic supercontinent Nuna. *Geology* 39 (5): 443–446. https://doi.org/10.1130/G31654.1.

Feldmann, R.M., A. Franțescu, O.D. Franțescu, A.A. Klompmaker, G. Logan Jr., C.M. Robins, C.E. Schweitzer, and D.A. Waugh. 2012. Formation of lobster-bearing concretions in the Late Cretaceous Bearpaw Shale, Montana, United States, in a complex geochemical environment. *Palaios* 27 (12): 842–856.

Fisher, Q.J., R. Raiswell, and J.D. Marshall. 1998. Siderite concretions from nonmarine shales (Westphalian A) of the Pennines, England: Controls on their growth and composition. *Journal of Sedimentary Research* 68 (5): 1034–1045.

Gaines, R.R., and J.S. Vorhies. 2016. Growth mechanisms and geochemistry of carbonate concretions from the Cambrian Wheeler Formation (Utah, USA). *Sedimentology* 63 (3): 662–698.

German, C.R., and H. Elderfield. 1990. Application of the Ce anomaly as a paleoredox indicator: The ground rules. *Paleoceanography* 5 (5): 823–833.

German, C.R., B.P. Holliday, and H. Elderfield. 1991. Redox cycling of rare earth elements in the suboxic zone of the Black Sea. *Geochimica et Cosmochimica Acta* 55 (12): 3553–3558.

Guo, H., Y.S. Du, L.C. Kah, J.H. Huang, C.Y. Hu, H. Huang, and W.C. Yu. 2013. Isotopic composition of organic and inorganic carbon from the Mesoproterozoic Jixian Group, North China: Implications for biological and oceanic evolution. *Precambrian Research* 224: 169–183.

Gutjahr, M., M. Frank, C.H. Stirling, V. Klemm, T. van de Flierdt, and A.N. Halliday. 2007. Reliable extraction of a deepwater trace metal isotope signal from Fe–Mn oxyhydroxide coatings of marine sediments. *Chemical Geology* 242 (3–4): 351–370.

Haley, B.A., G.P. Klinkhammer, and J. McManus. 2004. Rare earth elements in pore waters of marine sediments. *Geochimica et Cosmochimica Acta* 68 (6): 1265–1279.

Hendry, J.P., M.J. Pearson, N.H. Trewin, and A.E. Fallick. 2006. Jurassic septarian concretions from NW Scotland record interdependent bacterial, physical and chemical processes of marine mudrock diagenesis. *Sedimentology* 53 (3): 537–565.

Huggett, J.M., A.S. Gale, and S. Evans. 2000. Carbonate concretions from the London Clay (Ypresian, Eocene) of southern England and the exceptional preservation of wood-boring communities. *Journal of the Geological Society* 157: 187–200.

Johnson, K.S., W.M. Berelson, K.H. Coale, T.L. Coley, V.A. Elrod, W.R. Fairey, H. D. Iams, T.E. Kilgore, and J.L. Nowicki. 1992. Manganese flux from continental margin sediments in a transect through the oxygen minimum. *Science* 257 (5074): 1242–1245.

Kah, L.C., T.W. Lyons, and T.D. Frank. 2004. Low marine sulphate and protracted oxygenation of the Proterozoic biosphere. *Nature* 431 (7010): 834–838.

Kim, J.-H., M.E. Torres, B.A. Haley, M. Kastner, J.W. Pohlman, M. Riedel, and Y.-J. Lee. 2012. The effect of diagenesis and fluid migration on rare earth element distribution in pore fluids of the northern Cascadia accretionary margin. *Chemical Geology* 291: 152–165.

Liang, H.M., X. Chen, C.S. Wang, D.K. Zhao, and H. Weissert. 2016. Methane-derived authigenic carbonates of mid-Cretaceous age in southern Tibet: Types of carbonate concretions, carbon sources, and formation processes. *Journal of Asian Earth Sciences* 115: 153–169.

Lowenstein, T.K., M.N. Timofeeff, S.T. Brennan, L.A. Hardie, and R.V. Demicco. 2001. Oscillations in Phanerozoic seawater chemistry: Evidence from fluid inclusions. *Science* 294 (5544): 1086–1088.

Loyd, S.J., W.M. Berelson, T.W. Lyons, D.E. Hammond, A.K. Tripati, J.M. Eiler, and F.A. Corsetti. 2012. Formation mechanisms of carbonate concretions of the Monterey Formation: Analyses of clumped isotopes, iron, sulfur and carbon. *Mineralogical Magazine* 76: 2036–2036.

Loyd, S.J., J.A.D. Dickson, J.R. Boles, and A.K. Tripati. 2014. Clumped-isotope constraints on cement paragenesis in septarian concretions. *Journal of Sedimentary Research* 84 (12): 1170–1184.

Luo, Q.Y., N.N. Zhong, Y.N. Wang, L. Ma, and M. Li. 2015. Provenance and paleoweathering reconstruction of the Mesoproterozoic Hongshuizhuang Formation (1.4 Ga), northern North China. *International Journal of Earth Sciences* 104 (7): 1701–1720.

Lyons, T.W., C.T. Reinhard, and N.J. Planavsky. 2014. The rise of oxygen in Earth's early ocean and atmosphere. *Nature* 506 (7488): 307–315.

McCoy, V.E. 2014. Concretions as agents of soft-tissue preservation: A review. *The Paleontological Society Papers* 20: 147–162.

McLennan, S.M. 1989. Rare earth elements in sedimentary rocks: Influence of provenance and sedimentary processes. *Reviews in Mineralogy and Geochemistry* 21 (1): 169–200.

Meyer, R.L., N. Risgaard-Petersen, and D.E. Allen. 2005. Correlation between anammox activity and microscale distribution of nitrite in a subtropical mangrove sediment. *Applied and Environmental Microbiology* 71 (10): 6142–6149.

Mozley, P.S. 1989. Complex compositional zonation in concretionary siderite: Implications for geochemical studies. *Journal of Sedimentary Petrology* 59 (5): 815–818.

Mozley, P.S., and S.J. Burns. 1993. Oxygen and carbon isotopic composition of marine carbonate concretions: An overview. *Journal of Sedimentary Research* 63 (1): 73–83.

Planavsky, N., A. Bekker, O.J. Rouxel, B. Kamber, A. Hofmann, A. Knudsen, and T.W. Lyons. 2010. Rare earth element and yttrium compositions of Archean and Paleoproterozoic Fe formations revisited: New perspectives on the significance and mechanisms of deposition. *Geochimica et Cosmochimica Acta* 74 (22): 6387–6405.

Planavsky, N.J., C.T. Reinhard, X. Wang, D. Thomson, P. McGoldrick, R.H. Rainbird, T. Johnson, W.W. Fischer, and T.W. Lyons. 2014. Low mid-Proterozoic atmospheric oxygen levels and the delayed rise of animals. *Science* 346 (6209): 635–638.

Raiswell, R. 1988. Evidence for surface reaction-controlled growth of carbonate concretions in shales. *Sedimentology* 35 (4): 571–575.

Raiswell, R., S.H. Bottrell, S.P. Dean, J.D. Marshall, A. Carr, and D. Hatfield. 2002. Isotopic constraints on growth conditions of multiphase calcite–pyrite–barite concretions in Carboniferous mudstones. *Sedimentology* 49 (2): 237–254.

Raiswell, R., and Q.J. Fisher. 2000. Mudrock-hosted carbonate concretions: A review of growth mechanisms and their influence on chemical and isotopic composition. *Journal of the Geological Society* 157: 239–251.

Raiswell, R., and Q.J. Fisher. 2004. Rates of carbonate cementation associated with sulphate reduction in DSDP/ODP sediments: Implications for the formation of concretions. *Chemical Geology* 211 (1–2): 71–85.

Roberts, A.P., and R. Weaver. 2005. Multiple mechanisms of remagnetization involving sedimentary greigite (Fe_3S_4). *Earth and Planetary Science Letters* 231 (3–4): 263–277.

Saager, P.M., H.J.W. De Baar, and P.H. Burkill. 1989. Manganese and iron in Indian Ocean waters. *Geochimica et Cosmochimica Acta* 53 (9): 2259–2267.

Sellés-Martínez, J. 1996. Concretion morphology, classification and genesis. *Earth-Science Reviews* 41 (3–4): 177–210.

Tang, D.J., X.Y. Shi, G.Q. Jiang, T. Wu, J.B. Ma, and X.Q. Zhou. 2018. Stratiform siderites from the Mesoproterozoic Xiamaling Formation in North China: Genesis and environmental implications. *Gondwana Research* 58: 1–15.

Tang, D.J., X.Y. Shi, G.Q. Jiang, X.Q. Zhou, and Q. Shi. 2017. Ferruginous seawater facilitates the transformation of glauconite to chamosite: An example from the Mesoproterozoic Xiamaling Formation of North China. *American Mineralogist* 102 (11): 2317–2332.

Tang, D.J., X.Y. Shi, Q. Shi, J.J. Wu, G.Y. Song, and G.Q. Jiang. 2015. Organomineralization in Mesoproterozoic giant ooids. *Journal of Asian Earth Sciences* 107: 195–211.

Tang, D.J., X.Y. Shi, X.Q. Wang, and G.Q. Jiang. 2016. Extremely low oxygen concentration in mid-Proterozoic shallow seawaters. *Precambrian Research* 276: 145–157.

Thamdrup, B., and D.E. Canfield. 1996. Pathways of carbon oxidation in continental margin sediments off central Chile. *Limnology and Oceanography* 41 (8): 1629–1650.

Thamdrup, B., H. Fossing, and B.B. Jørgensen. 1994. Manganese, iron and sulfur cycling in a coastal marine sediment, Aarhus bay, Denmark. *Geochimica et Cosmochimica Acta* 58 (23): 5115–5129.

Tostevin, R., R.A. Wood, G.A. Shields, S.W. Poulton, R. Guilbaud, F. Bowyer, A. M. Penny, T. He, A. Curtis, K.H. Hoffmann, and M.O. Clarkson. 2016. Low-oxygen waters limited habitable space for early animals. *Nature Communications* 7: 12818. https://doi.org/10.1038/ncomms12818.

Trefry, J.H., B.J. Presley, W.L. Keeney-Kennicutt, and R.P. Trocine. 1984. Distribution and chemistry of manganese, iron, and suspended particulates in Orca Basin. *Geo-Marine Letters* 4 (2): 125–130.

Turekian, K.K., and K.H. Wedepohl. 1961. Distribution of the elements in some major units of the Earth's crust. *GSA Bulletin* 72 (2): 175–192.

Wang, X.M., S.C. Zhang, H.J. Wang, C.J. Bjerrum, E.U. Hammarlund, E.R. Haxen, J. Su, Y. Wang, and D.E. Canfield. 2017. Oxygen, climate and the chemical evolution of a 1400 million year old tropical marine setting. *American Journal of Science* 317 (8): 861–900.

Whiticar, M.J. 1999. Carbon and hydrogen isotope systematics of bacterial formation and oxidation of methane. *Chemical Geology* 161 (1–3): 291–314.

Zhang, S.C., X.M. Wang, E.U. Hammarlund, H.J. Wang, M.M. Costa, C.J. Bjerrum, J.N. Connelly, B.M. Zhang, L.Z. Bian, and D.E. Canfield. 2015. Orbital forcing of climate 1.4 billion years ago. *Proceedings of the National Academy of Sciences of the United States of America* 112 (12): E1406–E1413.

Zhang, S.C., X.M. Wang, H.J. Wang, C.J. Bjerrum, E.U. Hammarlund, M.M. Costa, J.N. Connelly, B.M. Zhang, J. Su, and D.E. Canfield. 2016. Sufficient oxygen for animal respiration 1,400 million years ago. *Proceedings of the National Academy of Sciences of the United States of America* 113 (7): 1731–1736.

Zhang, S.C., X.M. Wang, H.J. Wang, E.U. Hammarlund, J. Su, Y. Wang, and D.E. Canfield. 2017a. The oxic degradation of sedimentary organic matter 1400 Ma constrains atmospheric oxygen levels. *Biogeosciences* 14 (8): 2133–2149.

Zhang, S.H., Z.X. Li, D.A.D. Evans, H.C. Wu, H.Y. Li, and J. Dong. 2012. Pre-Rodinia supercontinent Nuna shaping up: A global synthesis with new paleomagnetic results from North China. *Earth and Planetary Science Letters* 353–354: 145–155.

Zhang, S.H., Y. Zhao, X.H. Li, R.E. Ernst, and Z.Y. Yang. 2017b. The 1.33–1.30 Ga Yanliao large igneous province in the North China Craton: Implications for reconstruction of the Nuna (Columbia) supercontinent, and specifically with the North Australian Craton. *Earth and Planetary Science Letters* 465: 112–125.

Zhang, S.H., Y. Zhao, Z.Y. Yang, Z.F. He, and H. Wu. 2009. The 1.35 Ga diabase sills from the northern North China craton: Implications for breakup of the Columbia (Nuna) supercontinent. *Earth and Planetary Science Letters* 288 (3–4): 588–600.